Ionic Conductivity and Structure of Glasses Synthesized by Mechanical-Milling Methods in the x[Na2S]–(100 – x) [0.5GeS2–0.5Ga2S3] System

Jiajie Zhang, Virginie Nazabal, David Le Coq, Laurent Calvez, Xianghua Zhang, Olivier Hernandez, Gwenhaël Duplaix-Rata, Corentin Poidevin, Xavier Rocquefelte, Eric Furet, et al.

▶ **To cite this version:**

Jiajie Zhang, Virginie Nazabal, David Le Coq, Laurent Calvez, Xianghua Zhang, et al.. Ionic Conductivity and Structure of Glasses Synthesized by Mechanical-Milling Methods in the x[Na2S]–(100 – x) [0.5GeS2–0.5Ga2S3] System. Inorganic Chemistry, 2023, Inorganic Chemistry, 62 (46), pp.19033-19042. 10.1021/acs.inorgchem.3c02849 . hal-04303379

HAL Id: hal-04303379
https://hal.science/hal-04303379

Submitted on 11 Dec 2023

HAL is a multi-disciplinary open access archive for the deposit and dissemination of scientific research documents, whether they are published or not. The documents may come from teaching and research institutions in France or abroad, or from public or private research centers.

L'archive ouverte pluridisciplinaire **HAL**, est destinée au dépôt et à la diffusion de documents scientifiques de niveau recherche, publiés ou non, émanant des établissements d'enseignement et de recherche français ou étrangers, des laboratoires publics ou privés.

Ionic conductivity and structure of glasses synthetized by mechanical milling methods in the x [Na_2S]– (100-x) [0.5GeS_2–0.5Ga_2S_3] system

Jiajie Zhang,[1] Virginie Nazabal,[1] David Le Coq,[1] Laurent Calvez,[1] Xiang-Hua Zhang,[1] Olivier Hernandez,[2] Gwenhael Duplaix-Rata,[1] Corentin Poidevin,[1] Xavier Rocquefelte,[1] Eric Furet,[1] Louisiane Verger*[1]

[1] Univ Rennes, CNRS, ISCR (Institut des Sciences Chimiques de Rennes) – UMR 6226, F-35000 Rennes, France

[2] Nantes Université, CNRS, Institut des Matériaux de Nantes Jean Rouxel, IMN, F-44000 Nantes, France

**louisiane.verger@univ-rennes.fr*

Abstract

Chalcogenide glasses in the Na_2S–GeS_2–Ga_2S_3 pseudo-ternary system were synthesized using a combination route of melt quenching and mechanical milling methods. Firstly, a glass rich in germanium (90GeS_2–10Ga_2S_3) is synthesized by melt-quenching synthesis in silica tube sealed under vacuum. This glass is used as a precursor for the second step of mechanochemistry to explore the Na_2S–GeS_2–Ga_2S_3 pseudo ternary system. By using this synthesis route, the glass forming ability is improved as the vitreous domain is enlarged, especially for Na and Ga rich compositions. The so-obtained amorphous powders are characterized by Raman spectroscopy, differential scanning calorimetry, X-ray total scattering and pair distribution function (PDF) analysis. The evolution of the

Raman features observed are reproduced using density functional theory calculations. Impedance spectroscopy was performed to determine the conductivity of the new glasses. The addition of germanium sulfide in the Na_2S–Ga_2S_3 pseudo binary enables to increase the conductivity of one order of magnitude. Best room-temperature ionic conductivity measured by impedance spectroscopy is reached at 1.8×10^{-5} $S.cm^{-1}$.

Key words

Chalcogenide glass, mechanical synthesis, sodium solid-state electrolyte, ionic conductivity.

1. Introduction

Sulfide-based glasses and glass-ceramics are well acknowledged for their high ionic conductivities compared to their oxide counterparts.[1,2] Furthermore, their machinability and wide compositional flexibility provide advantages to optimize the conductivity properties.[3,4] Used as solid-state electrolytes, chalcogenide glasses are considered a promising solution for a next-generation battery due to their simple structure and enhanced safety.[5,6] Although most current studies on solid-state batteries are based on lithium because of its high specific capacity, problems with lithium dendrite growth and the polysulfide shuttle effect make sodium-ion batteries stand out as a dark horse.[7–9] As the Na atom is heavier and larger than the Li atom, the gravimetric and volumetric energy densities of Na-ion batteries are not expected to exceed those of Li analogues.[10] However, this would not be considered a critical issue in large-scale industrial production, where battery cost and durability are the most important considerations.[11,12]

Various sulfide-based sodium solid electrolytes have been reported, such as the Na_3PS_4 glass-ceramic, which exhibits high conductivity at room temperature (2.0–4.6 × 10^{-4} $S.cm^{-1}$) as well as a wide electrochemical window (5 V).[13] Although numerous studies have been carried out on Na_2S-based system,[14–17] very few focus on the Na_2S–GeS_2–Ga_2S_3 pseudo-ternary, particularly obtained from mechanical milling. Yao *et al.* reported x [Na_2S]–(100-x) [0.9GeS_2–0.1Ga_2S_3] glass compositions obtained by melt-quenching technique, which used 90[GeS_2]–10[Ga_2S_3] as the basic glass former.[18,19] The difference in mole fraction between GeS_2 and Ga_2S_3 in the glass former is due to the difficulty of obtaining Ga-rich glasses using conventional melt-quenching synthesis. Gallium has a low reactivity with chalcogen elements during synthesis.

Mechanochemistry is a means of exploring chalcogenide glass compositions that cannot be obtained by the standard melt-quenching technique. For example, the Ga_2S_3 content has been increase up to 80 mol% in the Na_2S–Ga_2S_3 pseudo-binary.[20] The constant collision between the powder and the milling utensil (beads, pot) produces mechanical stress, triggering the accumulation of structural defects such as cation site disorder [21,22] or shearing and tearing, which ultimately lead to distortion of the geometric coordination.[23] In addition, mechanochemistry is an energy-efficient alternative method to the conventional synthesis of chalcogenide glasses in silica tubes sealed under vacuum. In recent years, the usage of mechanical ball milling to obtain solid state electrolytes and cathode materials has been booming due to the requirements of lower synthesis temperatures and increased production on an industrial scale.[24]

In this work, the strategy of using 50[GeS_2]–50[Ga_2S_3] as the basic glass former was chosen to study the impact of Ga_2S_3 on the glass forming ability and properties of the resulting material. Na_2S is added to study the x [Na_2S]–(100-x) [0.5GeS_2–0.5Ga_2S_3]

pseudo ternary. A hybrid synthesis route was chosen, using conventional melt-quenching technique and mechanochemistry. After complete amorphization of the powders, the thermal and structural properties of powdered glasses were investigated. Finally, the evolution of the ionic conductivity as a function of sample composition is discussed.

2. Materials and methods

2.1 Materials

The 90[GeS_2]–10[Ga_2S_3] glass was firstly prepared as a precursor by melt-quenching method. 15 g of stoichiometric proportions of germanium (Umicore, 5N), gallium (Neyco, 99.99%), and sulfur (Strem Chemical Inc., 6N) were added as starting materials. Solids were then melted and homogenized at 840 °C for 14 h in a silica tube sealed under vacuum. The glass melt was quenched in water at room temperature for several seconds.

A series of compositions was synthesized in the pseudo ternary x [Na_2S]–(100-x) [0.5GeS_2–0.5Ga_2S_3] with *x* from 10 to 75 mol% (**Table 1**). They are obtained by mechano-chemical milling using a planetary mill (Fritsch, Pulverisette 7). 5 g of combination of Na_2S (Alfa Aesar, 95% purity), 90[GeS_2]–10[Ga_2S_3] glass and Ga_2S_3 (synthesized according to our previous work [25]) are added proportionally into a zirconia bowl with ZrO_2 balls (diameter 3 mm, beads/powder mass ratio = 20/1). Every hour the bowl was opened, and materials were ground manually for the purpose of obtaining homogenous powders. The ball milling synthesis was conducted at a rotation speed of 600 rpm until total amorphization. Every step of the process is carefully controlled under a dry N_2 atmosphere. The samples are labeled in the rest of the article *x*Na, *x* being the molar content in Na_2S. Compositions investigated can be found in **Table 1**.

The amorphous powders were pressed into 10 mm diameter pellets under vacuum at a pressure of 2 tons for the Raman and impedance spectroscopies characterizations.

2.2 Thermal analyses

Powdered glass samples were weighted and sealed in hermetic aluminum pans in N_2 atmosphere. Glass transition temperature (T_g) and crystallization onset temperature (T_x) of all samples were characterized with a differential scanning calorimeter (DSC Q20 Thermal Analysis). All experiments were carried from 25 °C up to 530 °C with a heating rate of 10 °C. min^{-1}.

2.3 X-ray diffraction analyses

X-ray diffraction (XRD) patterns of amorphous and crystalline samples were measured at room temperature using a PANalytical X'pert Pro-diffractometer (Bragg−Brentano geometry, Cu-source, Ni-filter, $K\bar{\alpha}$ radiation, 40 kV, 40 mA, PIXcel 1D detector). The patterns were recorded in the 5–85° 2θ range with a step size of 0.0261°. A polyimide thin film was used during preparation to protect samples from air.

2.4 Raman spectroscopy

Raman scattering spectra of glass powder pellets were collected at room temperature under 532 nm laser excitation with a spectrometer coupled to a microscope and confocal aperture (HREvo-LabRam spectrometer, Horiba). To avoid photoinduced phenomena, optical density filters have been selected to reduce the laser power focused on the samples to few mW. To protect the samples from air, powder pellets were placed in aluminum pans covered by microscope glass slide using epoxy resin as glue to ensure air tightness. The Raman measurements were performed on a surface area of 60x60 μm^2 on a hundred points (1 second, 5 acquisitions) for each composition. The homogeneity of the Raman

spectrum over the whole area was checked for each sample and an average spectrum representative of the glass sample was considered and plotted.

2.5 Synchrotron X-ray total scattering/Pair Distribution function analysis

Synchrotron X-ray total scattering experiments were performed at room temperature on the XPDF I15-1 at Diamond synchrotron, using a radiation wavelenght of 0.16169 Å selected from a superconducting wiggler X-ray source by a bent Laue monochromator followed by a multi-layer mirror. The calibration and the wavelength determination was done using a silicon powder (NIST standard reference material 640d). Samples were loaded in sealed borosilicate glass capillaries with a diameter of 1 mm. Two frames of 600 s were collected for each sample in a high flux transmission mode using a large area detector (43.2×43.2 cm, PerkinElmer XRD 4343C) and then summed up to obtain a less noisy data set. An empty capillary was also measured to perform the background subtraction. The corresponding pair distribution function was calculated using PDFgetX3 with Q_{max} = 25.55 $Å^{-1}$.[26]

2.6 Conductivity measurements

Electrical conductivity measurements were performed with the help of Autolab workstation (PSTAT302N with FRA32M and ECD module) in a temperature range from 283 to 363 K with a frequency varying from 1 MHz down to 1Hz and a signal amplitude of 100 mV. To fulfill the impedance measurement, the as-prepared glass pellets were coated with Au thin layers on both sides. The coating was carried out using a low vacuum coater (EM ACE200; Leica Microsystems) which was installed in a N_2 filled glove box. Following one of the recommendations of Ohno et al.,[27] we carried out a series of

measurement on one of the composition synthesized in this work, 50Na, with 5 different pellet thicknesses, ranging from 0.6 to 1.87 mm. We found that conductivity for the same composition can vary from a factor 1.3 at room temperature to 3.2 at 90 °C. The thickness of the pellets used for impedance spectroscopy was therefore set at around 0.9 mm for sample comparison.

The electronic conductivity of glass pellets was measured using potentiostatic chronoamperometry. A constant potential difference (100 mV) was applied to a steel/glass pellet/sodium cell. The resulting current measured after stabilization is due to the electron motion.

2.7 Density functional calculations

Density Functional Theory (DFT) calculations were performed using ORCA suite of programs.[28,29] All the molecular models were fully optimized using the B3LYP functional.[30] The Kohn-Sham orbitals were expanded on the TZVPP Gaussian basis set.[31] The resulting optimized atomic structures were used to simulate harmonic Raman spectra by computing analytically the polarizability (Polar 1 and NumFreq flags).

3. Results and discussion

3.1 Glass-forming properties

Mechanical milling tests were first carried out to obtain the targeted glass compositions from elemental germanium. However, characteristic reflections of crystalline Ge were observed on XRD pattern even after extended milling time (10 h) and, more importantly,

their intensity did not decrease with additional milling time. Furthermore, the chosen basic glass former, 50[GeS_2]–50[Ga_2S_3], cannot be obtained by the conventional melt-quenching technique due to the low reactivity of Ga. A hybrid synthesis route was therefore applied: a 90[GeS_2]–10[Ga_2S_3] binary glass precursor was first synthesized by the conventional melt quenching process. Then, stoichiometric proportions of commercial Na_2S and Ga_2S_3, synthetized by our care, were added to the glass precursor to achieve the targeted compositions of x [Na_2S]–(100-x) [0.5GeS_2–0.5Ga_2S_3] and the mixture was mechanically milled.

The reaction process is monitored by powder XRD analysis at different milling times, as shown for the sample 70Na in **Fig.1a**. The disappearance of any crystalline phases peaks indicates complete amorphization. XRD patterns of samples 10Na to 75Na just after complete amorphization are plotted in **Fig.1b**. It is visible that the milling time leading to total amorphization varies from 4 to 20 h. No direct relationship is observed between milling time to achieve amorphization and Na content, as observed in the x [Na_2S] –(100-x) [Ga_2S_3] pseudo binary.[20] However, as a general trend, milling time is higher for the sample with the highest Na content. This was also observed in the Li_2S-Ga_2S_3-GeS_2 pseudo ternary.[32] To probe the Na content limit of the amorphous domain along the x [Na_2S] –(100-x) [0.5GeS_2–0.5Ga_2S_3] line, the composition with x = 80 was synthesized. In this case, applying an extended milling time does not result in complete amorphization, since peaks of a residual crystalline phase, corresponding to Na_2S (space group *Fm*-3*m*, JCPDS No. 03-0933), are still detected and their intensities do not change. Comparing the milling time of mechanosynthesis using 90[GeS_2]–10[Ga_2S_3] glass as precursor with that of pure mechanical milling, there is a significant reduction in time, between 63 and 96 %. [32] This indicates that using a combination of melt-quenching and ball-milling as a

synthesis route can significantly improve efficiency due to the difficult amorphization of Ge during mechanical milling.

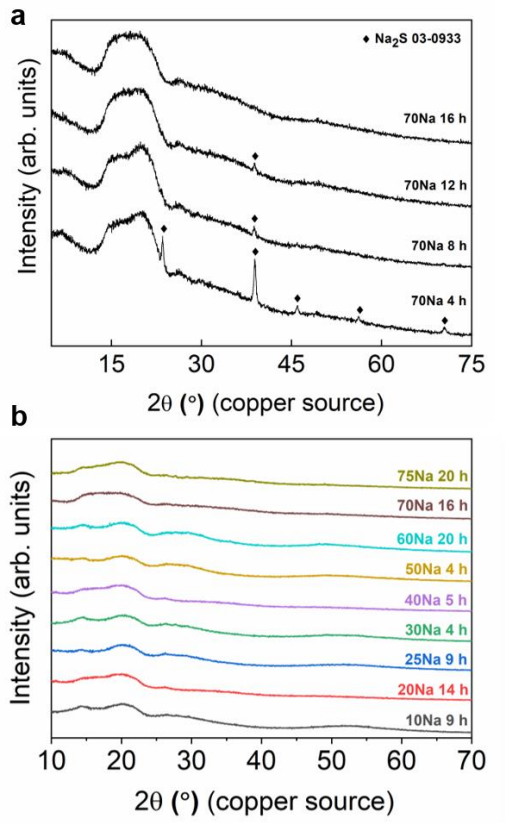

Figure 1. (a) XRD patterns of sample 70[Na_2S]-30[0.5GeS_2–0.5Ga_2S_3] (70Na) as a function of milling time (from bottom to top). **(b)** XRD patterns of samples x [Na_2S] –(100-x) [0.5GeS_2–0.5Ga_2S_3] prepared by ball milling and after reaching amorphization. The milling duration to reach amorphization is mentioned after the sample references. The broad shoulder peak at around 20 ° 2-theta that exists in all sample is due to the polyimide thin film.

3.2 Raman spectroscopy

The milling synthesis method is likely to generate more defects than parent glasses obtained by classical melting-quenching method and could induce deviation from a chemically ordered network model. Thus, to compare the local structure of glass powders by means of a relevant spectroscopy method, Raman scattering spectra were collected for the different chemical compositions (**Fig. 2a**).

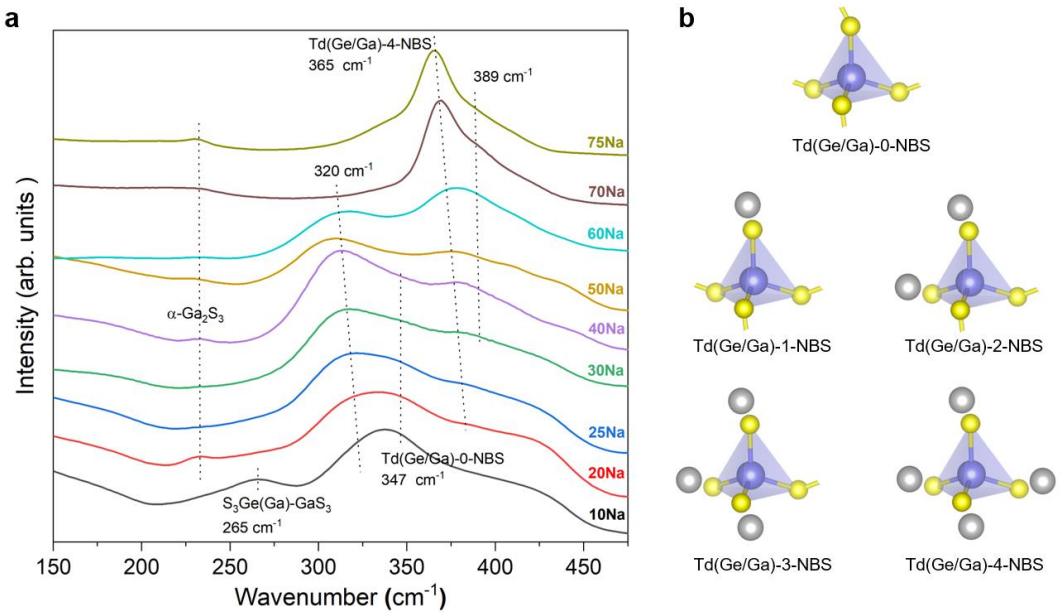

Figure 2. (a) Raman spectra of glass powders in the x [Na_2S]– (100-x) [0.5GeS_2–0.5Ga_2S_3] system, the Na_2S content increases from bottom to top. Key signals related with vibrations of 0-NBS and 4-NBS, Ge(Ga) –Ge(Ga) bonds and α-Ga_2S_3 are marked with dotted lines. (b) Schematic view of [$GeS_{4/2}$] or [$GaS_{4/2}$] tetrahedra, with 0 to 4 non-bridging sulfur (NBS), Ge or Ga atoms are in blue, S atoms in yellow and Na ions in grey.

Given the composition of the amorphous materials studied, x [Na_2S] – (100-x) [0.5GeS_2–0.5Ga_2S_3], we can start the description of the Raman spectra by considering the germanium sulfide-based system to which a high proportion of Ga_2S_3 is incorporated. This has a significant impact on the glass structure because the system will be deficient in sulfur and will therefore influences the vibrational modes of the lattice compared to that of GeS_2. The Ge-S glass system is known to be mainly formed by [$GeS_{4/2}$] tetrahedra linked by their corners and partly by edges in the case of stoichiometric glass GeS_2 forming a three-dimensional network structure.[33] In a free tetrahedral AB_4 molecule, there are two bond-stretching modes, the symmetric stretching mode ν_1 (A1, symmetry) only active in Raman, expected at 342 cm^{-1} and the asymmetric stretching mode ν_3 (F_2,

symmetry) at 388 cm^{-1}, which dominates the IR spectrum but is also active in Raman. In addition to the two bond-stretching modes, there are the two bond-bending modes, a ν_2 mode of E symmetry at 114 cm^{-1} which is only Raman active, and ν_4 mode (F_2 symmetry) at 147 cm^{-1} which is both IR and Raman active. For sulfur deficient glasses, germanium atoms can be linked by Ge-Ge homopolar bonds forming $GeS_{4-x}Ge_x$ (x=1, 2, 3 or 4) or $S_3Ge\text{-}GeS_3$ ethane-like structural units appearing usually at 258 cm^{-1}. Considering the system Ge-Ga-S, the glass network is constituted of $[GeS_{4/2}]$ and $[GaS_{4/2}]$ tetrahedra linked by corners and edges.[34–37] In the glass matrix considered, the introduction of a high proportion of Ga_2S_3 with a Ga/[Ge+Ga] ratio of 2/3 will create a high proportion of $[GaS_{2/4}]$ entities compared to $[GeS_{2/4}]$. As previously mentioned, this glass material will be a sulfur-deficient glass compared to stoichiometric GeS_2 glass. This sulfur deficiency can be expected to be compensated for by M-M bonds in this amorphous matrix, or by S^{2-} anion with a coordination number of 3.[38]

The spectrum of the sample with the lowest sodium concentration can be described in a first approach on the basis of a $50GeS_2\text{-}50Ga_2S_3$ glass matrix. The most intense peak at about 347 cm^{-1} is associated to the symmetric stretching mode of $\nu_1(A_1)[GeS_{4/2}]$ tetrahedra which are corner-shared (CS). The presence of edge-shared $[GeS_{4/2}]$ tetrahedra is revealed by their signatures at 372 cm^{-1}, although controversial, this assignment is reasonable and associated with medium-range order. The proportion in such Ge-based matrix is often proposed in the range of 10-20% for edge-shared (ES) compare to (CS) depending on composition.[37] Since Ge and Ga have nearly the same atomic masses and close binding energies, the vibration modes associated with these two types of tetrahedra (Td) $[GaS_{2/4}]$ and $[GeS_{2/4}]$ will be relatively close causing a widening of vibrational bands or an appearance of shoulders not very discernible. The symmetric vibration mode

$\nu_1(A_1)[GaS_{2/4}]$ Td is proposed to occur at 350 cm^{-1}.[35,36,39,40] The shoulder situated at 385-390 cm^{-1} corresponds to the asymmetric stretching mode $\nu_3(F_2)$ of the $[GeS_{4/2}]$ Td of weak intensity and vibration mode related to $[GaS_{2/4}]$ Td linked by their edge.[35] The large band at 405 cm^{-1} was also associated to $\nu_3(F_2)$ asymmetric stretching mode of the $[GeS_{4/2}]$ Td [41] and can be also associated to $[GaS_{4/2}]$ Td. The vibration mode of S_3Ge-S-GeS_3 units involving $[GeS_{4/2}]$ tetrahedra linked by their corner appear around 425 cm^{-1},[41] but was also proposed at 405 cm^{-1},[38] while those involving $[GeS_{4/2}]$ ES were proposed to appear at higher wavenumber.[38] Similar vibration modes S_3Ga-S-$Ga(Ge)S_3$ involving two $[GaS_{4/2}]$ tetrahedra or hybrid units composed of $[GeS_{4/2}]$ and $[GaS_{4/2}]$ can be expected in these energy range.[41,42] Finally, the vibrational modes corresponding to $(S)_3$-Ge-Ge-$(S)_3$ and $(S)_3$-Ge(Ga)-Ga-$(S)_3$ structural units including ethane-like units are observed around 258 and 269 cm^{-1}, respectively.[38,39,43] Insofar as some S atoms would present a three coordination by linking three structural units of type $[Ga(Ge)S_{4/2}]$, the Raman signature could not be clearly discerned among the other vibrational bands.[38]

With the continuous addition of Na_2S into $50Ga_2S_3$-$50GeS_2$ glass matrix, the Raman spectrum display three new peaks at around 320 cm^{-1}, 365 cm^{-1}, and 389 cm^{-1} and shoulders 411 cm^{-1} and 440 cm^{-1}. The aforementioned peaks are observed in the N_2S-$[0.1Ga_2S_3$-$0.9GeS_2]$ (N = Li, Na, K, Cs), Li_2S–GeS_2, K_2S–GeS_2, Cs_2S–GeS_2, Ag_2S–GeS_2, and CdS–Ga_2S_3-GeS_2 based glasses.[18,32,44,45] They can be attributed to vibration modes associated with $[GaS_4]$ and $[GeS_4]$ tetrahedra with different amounts of non-bridging sulfur (NBS). The structure of $NaS(Ge/Ga)S_{3/2}$, $(NaS)_2(Ge/Ga)S_{2/2}$, $(NaS)_3(Ge/Ga)S_{1/2}$ and $(NaS)_4(Ge/Ga)$ which corresponds to $[(Ge/Ga)S_{4/2}]$ tetrahedron basic unit with one, two, three and four NBS, respectively, are shown in **Fig. 2b**. The peak at 320 cm^{-1} appears first with increasing Na_2S content, while the vibrational bands associated with

[$Ga(Ge)S_{4/2}$] Td linked by their corners or edges around 347 cm^{-1} (which correspond to 0-NBS) are less and less discernible. Although clearly visible in samples up to x=60, the origin of this peak at 320 cm^{-1} in the Raman spectra is not clear from the literature. This peak could be associated with the formation of 1-NBS and 2-NBS, but these entities are generally proposed in the literature at 440 cm^{-1} and 411 cm^{-1}, respectively.

With increasing Na_2S content, the peak at 365 cm^{-1}, attributed to 4-NBS according to the literature, begins to amplify to eventually dominate the Raman spectrum. As a result, with increasing Na_2S content, the basic units of the Ga(Ge)-S tetrahedron gradually change from one non-bridging sulfur (NBS) to four NBS. The shoulder at 389 cm^{-1} is generally associated with 3-NBS according to the literature, but it could also be linked to the $S_3Ge(Ga)$-S-$Ge(Ga)S_3$ vibrational modes of tetrahedral units linked by corners or edges forming dimers or small clusters surrounded by Na^+. Indeed, the addition of Na_2S disconnects the sulfur bridges, and modify the medium range lattice and ultimately decrease the stability of the glass. For the samples 70Na and 75Na, the signal of 0-NBS is almost not detected. It should be noted that for samples 20Na, 40Na and 75Na, a low intensity signal assigned to α-Ga_2S_3 at 231 cm^{-1} is detected, due to the presence of impurity.

To help us with the interpretation of the different features discussed above, DFT calculations were performed. We have generated toys models based of one [$(Ge/Ga)S_4$] tetrahedron. The resulting singly bonded sulfur atoms were neutralized by adding hydrogen-like atoms with masses of germanium or gallium on a corner-sharing position. It should be noted that the resulting cluster is neutral for germanium, i.e. $Ge(SH)_4$, while not for gallium, i.e. $[Ga(SH)_4]^-$. These two models are thus composed of doubly bonded sulfur atoms, and thus correspond to 0-NBS. x-NBS models have been created by

replacing x hydrogen atoms by x sodium atoms (with x =1, 2, 3 and 4). The resulting optimized structures are shown in **Fig. 3a**. for $Ge(S[H_{1-x}Na_x])_4$. It evidences a systematic displacement of the sodium atoms away from the corner-sharing position, i.e. towards an edge or a face of the tetrahedron. **Fig. 3b** shows the Raman spectra simulations deduced from these optimized models for germanium.

The Raman spectra have been estimated after the application of a filter consisting to (i) isolate the vibrational modes of the five atoms constituting the tetrahedron (Ge or Ga, and 4 S) and (ii) select only the modes corresponding to forces larger than 0.2 a.u. In the case, of Ge clusters (**Fig. 3b**), the overall experimental features, reported in **Fig. 2**, are nicely reproduced. In particular, a symmetric stretching mode is simulated at 358 cm^{-1} for 0-NBS compared to 347 cm^{-1} for the experimental one, and is shifted towards lower wave numbers (335 and 329 cm^{-1} for 1-NBS and 2-NBS, respectively), and then to higher wave numbers (337 and 362 cm^{-1} for 3-NBS and 4-NBS, respectively). The evolution of the symmetrical elongation vibration mode ν_1, as a function of Na_2S content and non-bridging S formation, supports the hypothesis that 1-NBS and 2-NBS have a lower wavenumber signature and could thus explain the band appearance at 320 cm^{-1}. The 4-NBS vibration mode does indeed appear to be at a higher wavenumber than 0-NBS, while the association of 3-NBS is more delicate relying solely on DFT calculation. In contrast, the Raman simulations corresponding to the Ga clusters are altered. Indeed, while Ge clusters are neutral, Ga clusters have a net charge of minus one. Such a residual charge may influence the calculation of the polarizability and thus the Raman intensities. We cannot clearly link them to experimentally observed Raman vibration modes. Another approach needs to be developed for Ga entities.

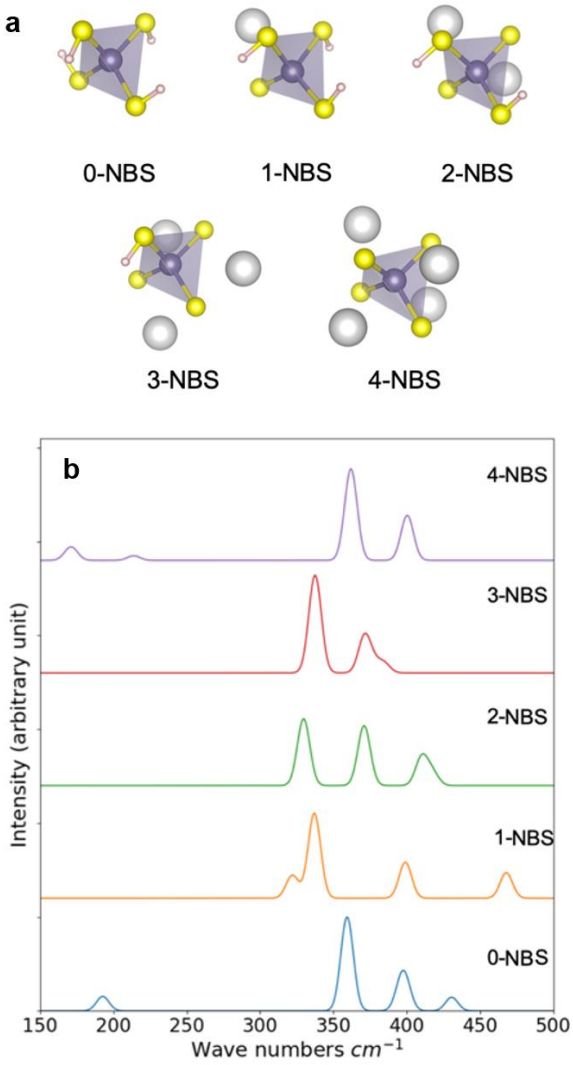

Figure 3: (a) Schematic representation of the optimized geometries of the $Ge(S[H_{1-x}Na_x])_4$ clusters (with x = 0, 1, 2, 3 and 4). Similar geometries have been obtained for $Ga[(S[H_{1-x}Na_x])_4]^-$ clusters. (b) DFT simulated Raman spectra of the $Ge(S[H_{1-x}Na_x])_4$ clusters. For Ge clusters, the Raman intensities have been normalized to the most intense peak of the related 0-NBS spectrum.

3.3 Pair Distribution Function Analysis

Synchrotron X-ray total scattering measurements were performed to probe the local structure of the obtained glasses. Experimental PDFs are extracted and represented in **Fig. 4** for samples 30Na and 50Na. The observed PDFs are overall similar to the one obtained on $NaGaS_2$ glass (using a laboratory X-ray diffractometer, Ag K_α radiation)

from our previous work on the pseudo binary x[Na_2S]-(100-x)[Ga_2S_3] without Ge,[46] although much less noisy and slightly better resolved in r (by 0.04 Å for the first PDF peak) owing to the use of a dedicated PDF synchrotron beamline. In the medium range order above 10 Å, no distinct peaks are observed, typical of amorphous materials (**Fig. 4a**). A closer look at the short-range order below 7 Å (**Fig. 4b**) reveals the present of two main peaks, at about 2.25 Å and 3.64 Å. The only crystalline composition existing in the pseudo ternary Na_2S-Ga_2S_3-GeS_2 is $Na_2Ga_2GeS_6$, corresponding to x = 100/3 in the notation x [Na_2S]–(100-x) [0.5GeS_2–0.5Ga_2S_3].[47] This composition is used as a reference to interpret the experimental PDFs obtained on glasses 30Na and 50Na.

Ga and Ge are located in T_d environment in $Na_2Ga_2GeS_6$, with Ga-S and Ge-S distances ranging from 2.24 to 2.28 Å and from 2.22 to 2.24 Å, respectively. The first peak observed in the PDF is then attributed to (Ga/Ge)-S distances, as in $NaGaS_2$ glass.[46] A clear difference of intensity is observed for this PDF peak between the 30Na and 50Na samples (see **Fig. 4b**), feature reproduced in the RDF (Radial Distribution Function) function derived from $G(r)$, the PDF function. The integrated intensity of the RDF peak at $r = 2.26$ Å is estimated to decrease by 18% from $x = 30$ to $x = 50$. The peak width being the same in both cases (0.21 Å), this peak area decrease could be tentatively interpreted as a decrease of coordination number in sulfur around Ga or Ge atoms upon rising x, the Na_2S content. The second peak is attributed to S-S distances within [GaS_4] and [GeS_4] tetrahedra, and to Ga-Ge, Ga-Ga or Ge-Ge distances between two tetrahedra connected by edges or corners.

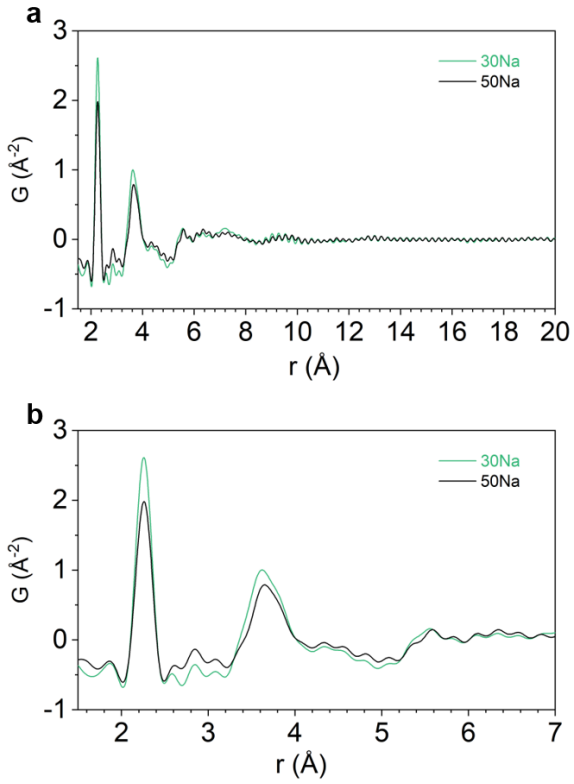

Figure 4. **(a)** X-ray PDFs of the 30 [Na_2S]– 70 [0.5GeS_2–0.5Ga_2S_3] (30Na, green) and the 50 [Na_2S]– 50 [0.5GeS_2–0.5Ga_2S_3] (50Na, black) glass powders. **(b)** Short range region of the PDFs up to 7 Å.

3.4 Thermal properties

The typical temperatures T_g and T_x of the amorphous samples are investigated and gathered in **Table 1**. A typical DSC measure, corresponding to 70Na after 16 h of milling is also shown in **Fig. 5a**. Both T_g and T_x show a rapid decrease with increasing Na_2S content (**Fig. 5b)**. This is due to the constant collapse of the mid-range network into local short-range network. The T_g and T_x stabilize when Na_2S content reaches the limit of the glass forming region. From the previous Raman result, the glass structure is filled mainly by 4-NBS in samples 70Na and 75Na. T_g reported for glasses using [0.1Ga_2S_3-0.9GeS_2] as a basic glass former in the literature is 20 to 120 °C lower than T_g reported in this study

using [$0.5Ga_2S_3$-$0.5GeS_2$] and the difference between the two system decreases with increasing Na_2S content [18]. This suggests that the addition of Ga_2S_3 leads to a more efficient interconnection in the glassy network and Ga_2S_3 acts as a glass former.

The value of ΔT (**Table 1**), which is equals to the difference between T_x and T_g, is critical to assess the thermal stability of glasses. In practice, a glass is considered thermally stable when ΔT is above 100 °C. ΔT firstly shows an upward trend, reaching a maximum of 122 °C for sample 40Na (**Fig. 5c**). But ΔT starts to decrease with increasing alkali content in the glass system until reaching the minimum of 33 °C for sample 75Na. This behavior is in line with expectations, as other Ge-Ga-S based glassy systems have shown a similar trend, including previous work on GeS_2–Ga_2S_3–NaX systems (with X = Cl or I) [48], GeS_2–Ga_2S_3–CsCl or CsI system [48,49], and lithium analogue GeS_2–Ga_2S_3–LiCl [50]. This can be explained by the fact that the constant addition of alkalis to the glass system results in the continuous rupture of Ga (Ge)–S–(Ge) Ga bonds and the formation of Ga (Ge)–S–Na bonds instead, ultimately leading to the degradation of glass network connectivity.

Table. 1 Summary of samples studied with sample references, composition in mol%, T_g, T_x, ΔT ($=T_x-T_g$) in °C, and ΔE_a in $kJ.mol^{-1}$. The conductivity of sample 10Na was too low to be measured with accuracy.

Sample reference	**Na_2S (mol%)**	**($0.5GeS_2$–$0.5Ga_2S_3$) (mol%)**	***T_g* (°C) (± 2 °C)**	***T_x* (°C) (± 2 °C)**	**ΔT (°C) (± 4 °C)**	**ΔE_a *(kJ/mol)***
10Na	10	90	445	505	60	/
20Na	20	80	450	497	47	44.27 ± 0.40
25Na	25	75	443	490	47	40.87 ± 0.45
30Na	30	70	410	491	81	44.85 ± 0.55
40Na	40	60	348	470	122	49.00 ± 1.1
50Na	50	50	320	403	83	47.62 ± 1.25
60Na	60	40	285	352	67	37.28 ± 0.43

70Na	70	30	255	294	39	34.83 ± 0.47
75Na	75	25	253	286	33	35.95 ± 0.07

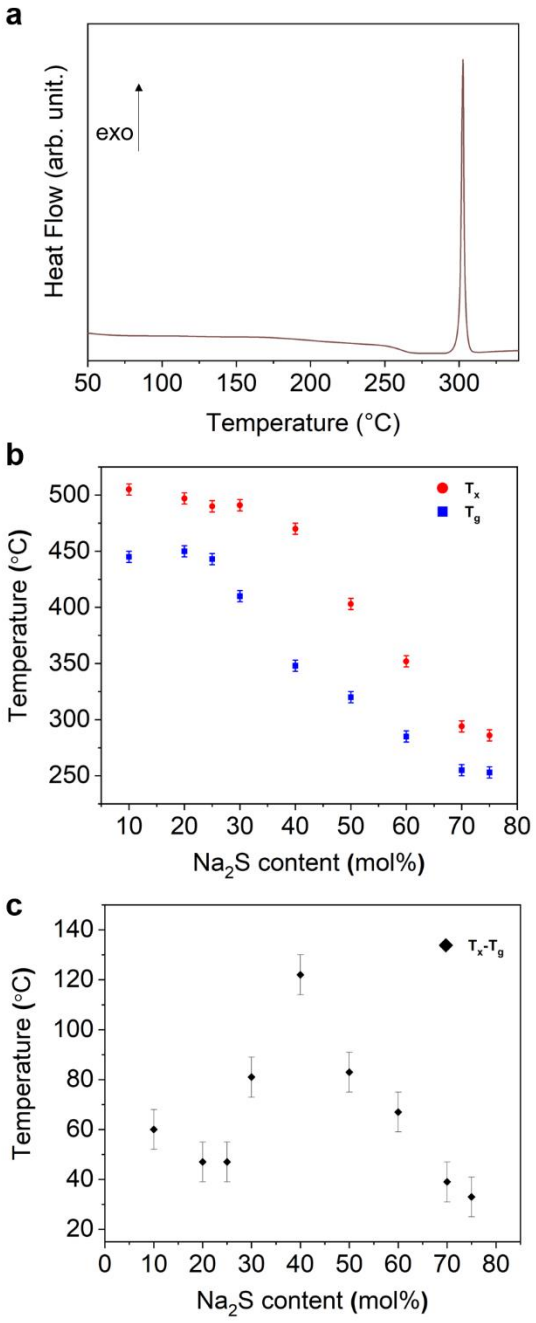

Figure 5. DSC analysis: **(a)** DSC trace of sample 70Na. T_g, T_x **(b)** and ΔT (=T_x-T_g) **(c)** of amorphous x [Na_2S]–(100-x) [0.5GeS_2–0.5Ga_2S_3] plotted as a function of x (Na_2S content) in mol%.

3.5 Electrical conductivity properties

The electrical conductivity of the samples was determined using a Nyquist plot where the imaginary part of the complex impedance is plotted against the real part of the complex impedance on the *x*-axis.[51] **Fig. 6** shows an example of a Nyquist plot for samples 40Na, 50Na and 70Na at room temperature. The semicircle in the high- and mid-frequency region represents the impedance of the sample. At the low-frequency region, the presence of a polarization tail results from the accumulation of charge carriers (Na^+) at the pellet-electrode interface, and indicates that the electrical conductivity is predominantly ionic.[52] Ideally, the spectrum in a Nyquist representation of a pressed powder ionic conductive should be characterized by two well-resolved semicircles and a polarization tail. The semicircle at higher frequency corresponds to the ionic transport in the grain, and the semi-circle at lower frequency corresponds to the grain boundary contribution. However, bulk and grain boundary contributions cannot be deconvoluted at room temperature and at 10 °C, as typically observed on such materials.[20,27] Therefore, the reported conductivity values correspond to the total conductivities of the sample and their corresponding activation barriers.

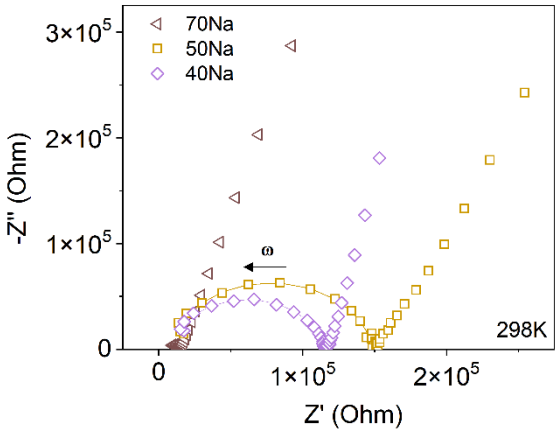

Figure 6. Nyquist plot of electrical impedance measurement of amorphous samples 70Na, 50Na, and 40Na at T = 298 K. The line corresponds to the semicircle fit.

The impedance of the samples was measured by fitting the semicircle, when it can be measured. For samples with the highest conductivity, the semicircle was not fully detected due to the upper frequency limitation of our device (1 MHz), and the impedance was estimated using the intersection of the polarization tail and the *x*-axis. Conductivity is therefore underestimated in this case. The conductivities of pressed pellets are not usually reported with error bars in the literature, as the uncertainty on the measurement arises from many different factors: from the sample itself (particle size, sample heterogeneity, pressure applied during shaping, etc) or from the measurement (coating on the pellets, pressure applied during measurement, impedance analyzer, etc). [27]

Fig. 7a shows the evolution of the conductivity of glass samples from 20Na to 75Na as a function of reverse temperature. The conductivity of all studied samples is calculated from the equation below:

$$\sigma = \frac{t}{R \times A} \qquad (1)$$

where σ is the conductivity (S.cm^{-1}), R is the sample resistance (Ohm), t is the pellet thickness (cm) and A is the pellet surface (cm^2).

As expected, the conductivity increases with the Na_2S content regardless of the temperature. The highest room-temperature conductivity, corresponding to sample 75Na, is reached at $\sigma = 1.8 \times 10^{-5}$ S.cm^{-1}. The highest conductivity, $\sigma = 1.0 \times 10^{-3}$ S.cm^{-1}, is obtained at 90 °C, for the same sample. For all diagrams obtained at different temperatures, the temperature (*T*) dependent ionic conductivity follows an Arrhenius law:

$$\sigma(T) = \frac{\sigma_0}{T} \times \exp\left(-\frac{\Delta E_a}{RT}\right) \quad (2)$$

where σ_0 is the pre-exponential factor (S.cm^{-1}.K), T is the temperature (K), ΔE_a is the activation energy (J.mol^{-1}), and R is the universal gas constant. ΔE_a are summarized in **Table 1**. It is in the same range than other sulfide-based Na^+ conductors.[19] There is no clear trend between the ΔE_a values and the Na content, although the highest values are reached for sample 40Na and 50Na.

Fig. 7b shows the Na_2S dependence of the ionic conductivity of the glass powders at room temperature. The ionic conductivity shows a greater increase when the Na_2S content goes from x=20 to 30, then the increase slows down as the Na_2S content enters in the range of x=40 to 60 and the range of x=70 to 75. The sample 60Na was synthesized twice, and the Raman spectroscopy and conductivity measurements were well reproduced. As the previous Raman analysis show, between 20Na and 40Na the structure is going through the network collapse as the intensity of the signal of 0-NBS is diminishing. This structure modification process might be the reason why the conductivity increases. The conductivity increases when Na_2S content rises from x=60 to 70 and 75. This can be

explained by the appearance of the contribution of 4-NBS entities in the 70Na and 75Na samples, as shown by Raman spectroscopy **(Fig. 2).**

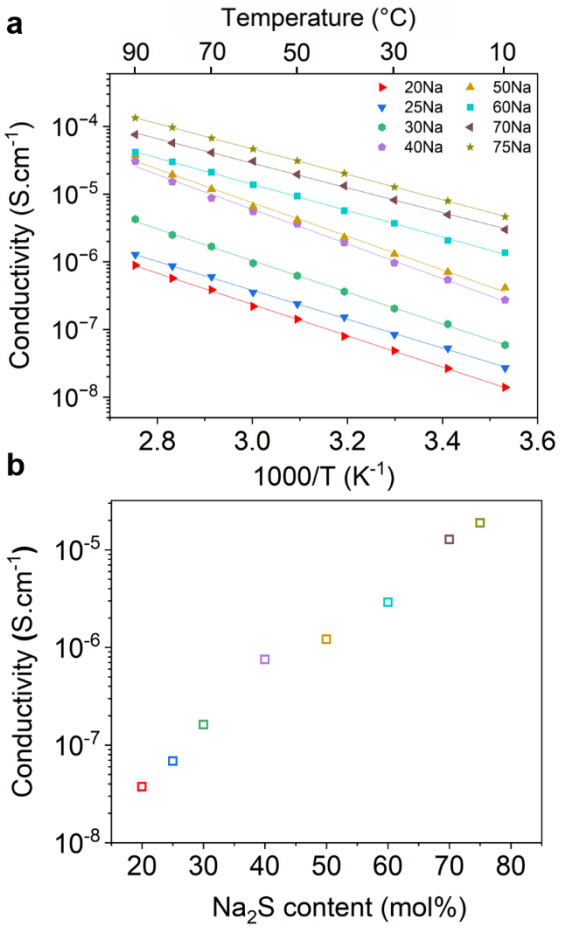

Figure 7. (a) Evolution of the temperature-dependent conductivity of cold-pressed glass powders. **(b)** Evolution of composition-dependent conductivity of cold-pressed glass powders at 25°C.

A solid electrolyte must have a high ionic conductivity, and low electronic conductivity in a ratio of at least 10^3. The electronic contribution σ_e to the total conductivity of samples with the highest ionic conductivity (70Na and 75Na) was measured using potentiostatic chronoamperometry, and calculated using Eq. 3:

$$\sigma_e = \frac{I_\infty \times t}{U \times A} \qquad (3)$$

where I_∞ is the residual current (A), t the pellet thickness (cm), U the voltage (V) and A the pellet surface area (cm^2). A typical measurement is shown in **Fig. 8** on sample 70Na. The calculated value of values of σ_e are 5.1 x 10^{-7} $S.cm^{-1}$ and 3.5 x 10^{-7} $S.cm^{-1}$ for samples 70Na and 75Na, respectively. They are in the same order of magnitude (10^{-7} $S.cm^{-1}$), and only 10 to 100 times lower than the ionic contribution. Further investigations must be devoted to investigate the origin of the electronic contribution in such material, and to decrease it.

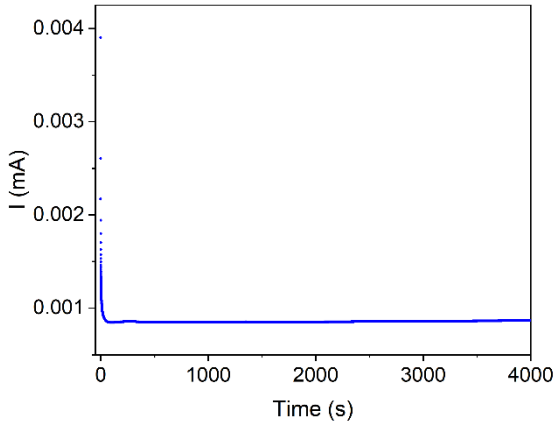

Figure 8. Potentiostatic chronoamperometric measurement on sample 70Na.

The room-temperature conductivities of bulk and powdered glasses with similar composition are summarized from the literature in **Table 2**. Comparing with samples in this work, generally the conductivity of bulk glasses is merely 1 to 4 times higher than that of glass powders which is within expectation. The mechano-synthesized then cold-pressed pellets show a lower ionic conductivity mainly because of the existing vacant spaces and grain boundaries between particles which hinder the mobility of cations. Comparing the mechano-synthesized powders of the binary Na_2S–Ga_2S_3 with this work, the ternary samples with similar Na_2S-content shows an increase up to 12 times higher

conductivity than that of the binary. Ga/Ge substitution is then an effective way to optimize the ionic conductivity.

Table. 2. Comparison of room-temperature ionic conductivity of the glass powders in this work with that of the bulk glass and glass powders reported in the literature.

Our work					***Literature***				
Na_2S (mol%)	GeS_2 (mol%)	Ga_2S_3 (mol%)	Sample properties	**σ (S.cm^{-1})**	Na_2S (mol%)	GeS_2 (mol%)	Ga_2S_3 (mol%)	Sample properties/Ref.	**σ (S.cm^{-1})**
40	30	30	Cold-pressed pellets	**7.6×10^{-7}**	*40*	*54*	*6*	*Bulk glass, Ref.*[19]	***1.8×10^{-6}***
50	25	25	Cold-pressed pellets	**1.1×10^{-6}**	*50*	*45*	*5*	*Bulk glass, Ref.*[19]	***5.1×10^{-6}***
60	20	20	Cold-pressed pellets	**1.4×10^{-6}**	*60*	*36*	*4*	*Bulk glass, Ref.*[19]	***7.1×10^{-6}***
70	15	15	Cold-pressed pellets	**1.2×10^{-5}**	*70*	*0*	*30*	*Cold-pressed pellet, Ref.*[20]	***9.1×10^{-7}***
75	12.5	12.5	Cold-pressed pellets	**1.8×10^{-5}**	*80*	*0*	*20*	*Cold-pressed pellet, Ref.* [20]	***1.9×10^{-6}***

4. Conclusion

Powdered glass samples were obtained in the x $[Na_2S]$– (100-x) $[0.5GeS_2–0.5Ga_2S_3]$ system, with *x* ranging from 10 to 75. The chosen synthesis route using melt-quenching method and mechanochemistry enables new glass compositions to be explored, particularly for Ga- and Na-rich compositions. Raman spectroscopy was used to study the glass structure as a function of Na_2S content. It reveals a steady collapse of $Ga(Ge)S_{4/2}$ tetrahedron-based medium-range network with the introduction of Na_2S, and the formation of non-bridging sulfur in the glass network. A feature at 320 cm^{-1} is detected, which becomes predominant for x=40 and is detected up to x=60. This feature could be associated with 1-NBS and 2-NBS. DFT calculations performed are consistent with this hypothesis. PDF analysis reveals that the local structure of the glass is similar to $NaGaS_2$

glass. Ionic conductivities of glass powders are measured. As expected, the ionic conductivity increases with the addition of Na_2S. Moreover, the specific transitions of dominant structure from 0-NBS to 4-NBS detected by Raman spectroscopy cause the conductivity surge of glass samples. The highest room-temperature conductivity is achieved for the sample with x=75 ($\sigma = 1.8 \times 10^{-5}$ S.cm^{-1} at room temperature), for which the predominance of 4-NBS entities is detected by Raman spectroscopy. The conductivities obtained in this work, which are from cold-pressed pellets, are comparable with that of the bulk glasses using a different glass network reported from the literature. Consequently, the addition of Ga_2S_3 does not improved the ionic conductivity of the samples. However, the addition of GeS_2 in the Na_2S-Ga_2S_3 glass system improves the conductivity by one order of magnitude for identical Na_2S content.

Acknowledgements

We thank Diamond Light Source for the access to beamline I15-1 and Dr. Philip A. Chater, Dr. Maria Diaz-Lopez and Dr. Daniel Irving for the X-ray total scattering experiment (proposal CY31861-1). L. V. was supported by Rennes Métropole (AIS grant). This publication is (partially) supported by the European Union through the European Regional Development Fund (ERDF), the Ministry of Higher Education and Research, the French region of Brittany and Rennes Métropole.

Declaration of Competing Interest

The authors declare that they have no known competing financial interests or personal relationships that could have appeared to influence the work reported in this paper.

References

(1) Zhang, Q.; Cao, D.; Ma, Y.; Natan, A.; Aurora, P.; Zhu, H. Sulfide-Based Solid-State Electrolytes: Synthesis, Stability, and Potential for All-Solid-State Batteries. *Adv. Mater.* **2019**, *31* (44), 1–42.

(2) Wu, J.; Liu, S.; Han, F.; Yao, X.; Wang, C. Lithium/Sulfide All-Solid-State Batteries Using Sulfide Electrolytes. *Adv. Mater.* **2021**, *33* (6).

(3) Takada, K.; Inada, T.; Kajiyama, A.; Kouguchi, M.; Sasaki, H.; Kondo, S.; Michiue, Y.; Nakano, S.; Tabuchi, M.; Watanabe, M. Solid State Batteries with Sulfide-Based Solid Electrolytes. *Solid State Ionics* **2004**, *172* (1-4 SPEC. ISS.), 25–30.

(4) Nam, Y. J.; Oh, D. Y.; Jung, S. H.; Jung, Y. S. Toward Practical All-Solid-State Lithium-Ion Batteries with High Energy Density and Safety: Comparative Study for Electrodes Fabricated by Dry- and Slurry-Mixing Processes. *J. Power Sources* **2018**, *375*, 93–101.

(5) Tatsumisago, M.; Hayashi, A. Chalcogenide Glasses as Electrolytes for Batteries. In *Chalcogenide Glasses*; 2013.

(6) Bokova, M.; Paraskiva, A.; Kassem, M.; Alekseev, I.; Bychkov, E. Tl2S-GeS-GeS2 System: Glass Formation, Macroscopic Properties, and Charge Transport. *J. Alloys Compd.* **2019**, *777*, 902–914.

(7) Lin, Z.; Liang, C. Lithium-Sulfur Batteries: From Liquid to Solid Cells. *J. Mater. Chem. A* **2015**, *3* (3), 936–958.

(8) Judez, X.; Zhang, H.; Li, C.; Eshetu, G. G.; González-Marcos, J. A.; Armand, M.; Rodriguez-Martinez, L. M. Review—Solid Electrolytes for Safe and High Energy Density Lithium-Sulfur Batteries: Promises and Challenges. *J. Electrochem. Soc.* **2018**, *165* (1), A6008–A6016.

(9) Manthiram, A.; Yu, X.; Wang, S. Lithium Battery Chemistries Enabled by Solid-State Electrolytes. *Nat. Rev. Mater.* **2017**, *2* (4).

(10) Xu, G. L.; Amine, R.; Abouimrane, A.; Che, H.; Dahbi, M.; Ma, Z. F.; Saadoune, I.; Alami, J.; Mattis, W. L.; Pan, F.; Chen, Z.; Amine, K. Challenges in Developing Electrodes, Electrolytes, and Diagnostics Tools to Understand and Advance Sodium-Ion Batteries. *Advanced Energy Materials*. 2018.

(11) Pan, H.; Hu, Y. S.; Chen, L. Room-Temperature Stationary Sodium-Ion Batteries for Large-Scale Electric Energy Storage. *Energy and Environmental Science*. 2013, pp 2338–2360.

(12) Bella, F.; Colò, F.; Nair, J. R.; Gerbaldi, C. Photopolymer Electrolytes for Sustainable, Upscalable, Safe, and Ambient-Temperature Sodium-Ion Secondary Batteries. *ChemSusChem* **2015**, *8* (21), 3668–3676.

(13) Wang, Y.; Song, S.; Xu, C.; Hu, N.; Molenda, J.; Lu, L. Development of Solid-State Electrolytes for Sodium-Ion Battery–A Short Review. *Nano Mater. Sci.* **2019**, *1* (2), 91–100.

(14) Souquet, J. L.; Robinel, E.; Barrau, B.; Ribes, M. Glass Formation and Ionic Conduction in the M_2S-GeS_2 (M = Li, Na, Ag) Systems. *Solid State Ionics* **1981**, *3–4* (C), 317–321.

(15) Ribes, M.; Barrau, B.; Souquet, J. L. Sulfide Glasses: Glass Forming Region, Structure and Ionic Conduction of Glasses in Na_2S-XS_2 (X=Si; Ge), Na_2S-P_2S_5 and Li_2S-GeS_2 Systems. *J. Non. Cryst. Solids* **1980**, *38–39* (PART 1), 271–276.

(16) Chu, I. H.; Kompella, C. S.; Nguyen, H.; Zhu, Z.; Hy, S.; Deng, Z.; Meng, Y. S.; Ong, S. P. Room-Temperature All-Solid-State Rechargeable Sodium-Ion Batteries with a Cl-Doped Na_3PS_4 Superionic Conductor. *Sci. Rep.* **2016**, *6* (1), 1–10.

(17) Zhang, Z.; Ramos, E.; Lalère, F.; Assoud, A.; Kaup, K.; Hartman, P.; Nazar, L. F. $Na_{11}Sn_2PS_{12}$: A New Solid State Sodium Superionic Conductor. *Energy Environ. Sci.* **2018**, *11* (1), 87–93.

(18) Yao, W.; Berg, K.; Martin, S. Structure and Properties of Glasses in the MI + M_2S + (0.1Ga_2S_3 +

$0.9GeS_2$), M = Li, Na, K and Cs, System. *J. Non. Cryst. Solids* **2008**, *354* (18), 2045–2053.

(19) Yao, W.; Martin, S. W. Ionic Conductivity of Glasses in the MI + M_2S + ($0.1Ga_2S_3$ + $0.9GeS_2$) System (M = Li, Na, K and Cs). *Solid State Ionics* **2008**, *178* (33–34), 1777–1784.

(20) Dénoue, K.; Le Coq, D.; Calers, C.; Gautier, A.; Verger, L.; Calvez, L. New Synthesis Route for Glasses and Glass-Ceramics in the Ga_2S_3-Na_2S Binary System. *Mater. Res. Bull.* **2021**, *142*, 111423.

(21) Delogu, F.; Mulas, G.; Schiffini, L.; Cocco, G. Mechanical Work and Conversion Degree in Mechanically Induced Processes. *Mater. Sci. Eng. A* **2004**, *382* (1–2), 280–287.

(22) Humphry-Baker, S. A.; Garroni, S.; Delogu, F.; Schuh, C. A. Melt-Driven Mechanochemical Phase Transformations in Moderately Exothermic Powder Mixtures. *Nat. Mater.* **2016**, *15* (12), 1280–1286.

(23) Liu, D.; Lei, W.; Qin, S.; Hou, L.; Liu, Z.; Cui, Q.; Chen, Y. Large-Scale Synthesis of Hexagonal Corundum-Type In_2O_3 by Ball Milling with Enhanced Lithium Storage Capabilities. *J. Mater. Chem. A* **2013**, *1* (17), 5274–5278.

(24) Suzuki, K.; Kato, D.; Hara, K.; Yano, T. aki; Hirayama, M.; Hara, M.; Kanno, R. Composite Sulfur Electrode Prepared by High-Temperature Mechanical Milling for Use in an All-Solid-State Lithium–Sulfur Battery with a $Li_{3.25}Ge_{0.25}P_{0.75}S_4$ Electrolyte. *Electrochim. Acta* **2017**, *258*, 110–115.

(25) Dénoue, K.; Cheviré, F.; Calers, C.; Verger, L.; Le Coq, D.; Calvez, L. Mechanochemical Synthesis and Structural Characterization of Gallium Sulfide Ga_2S_3. *J. Solid State Chem.* **2020**, *292*, 121743.

(26) Juhás, P.; Davis, T.; Farrow, C. L.; Billinge, S. J. L. PDFgetX3: A Rapid and Highly Automatable Program for Processing Powder Diffraction Data into Total Scattering Pair Distribution Functions. *urn:issn:0021-8898* **2013**, *46* (2), 560–566.

(27) Ohno, S.; Bernges, T.; Buchheim, J.; Duchardt, M.; Hatz, A. K.; Kraft, M. A.; Kwak, H.; Santhosha, A. L.; Liu, Z.; Minafra, N.; Tsuji, F.; Sakuda, A.; Schlem, R.; Xiong, S.; Zhang, Z.; Adelhelm, P.; Chen, H.; Hayashi, A.; Jung, Y. S.; Lotsch, B. V.; Roling, B.; Vargas-Barbosa, N. M.; Zeier, W. G. How Certain Are the Reported Ionic Conductivities of Thiophosphate-Based Solid Electrolytes? An Interlaboratory Study. *ACS Energy Lett.* **2020**, *5* (3), 910–915.

(28) Neese, F.; Wiley, J. Software Focus The ORCA Program System PROGRAM DESIGN. *WIREs Comput Mol Sci* **2012**, *2*, 73–78.

(29) Neese, F. Software Update: The ORCA Program System, Version 4.0. *WIREs Comput Mol Sci* **2018**, *8*, 1327.

(30) Becke, A. D. Density-functional Thermochemistry. I. The Effect of the Exchange-only Gradient Correction. *J. Chem. Phys.* **1992**, *96* (3), 2155–2160.

(31) Schäfer, A.; Horn, H.; Ahlrichs, R. Fully Optimized Contracted Gaussian Basis Sets for Atoms Li to Kr. *J. Chem. Phys.* **1992**, *97* (4), 2571–2577.

(32) Fan, B.; Fu, H.; Li, H.; Xue, B.; Zhang, X.; Luo, Z.; Ma, H. Ionic Conductive GeS_2-Ga_2S_3-Li_2S-LiI Glass Powders Prepared by Mechanical Synthesis. *J. Alloys Compd.* **2018**, *740*, 61–67.

(33) Tronc, P.; Bensoussan, M.; Brenac, A.; Sebenne, C. Optical-Absorption Edge and Raman Scattering in Ge_xSe_{1-x} Glasses. *Phys. Rev. B* **1973**, *8* (12), 5947.

(34) Loireau-Lozac'h, A. M.; Keller-Besrest, F.; Bénazeth, S. Short and Medium Range Order in Ga-Ge-S Glasses: An X-Ray Absorption Spectroscopy Study at Room and Low Temperatures. *J. Solid State Chem.* **1996**, *123* (1), 60–67.

(35) Julien, C.; Barnier, S.; Massot, M.; Chbani, N.; Cai, X.; Loireau-Lozac'h, A. M.; Guittard, M. Raman and Infrared Spectroscopic Studies of Ge-Ga-Ag Sulphide Glasses. *Mater. Sci. Eng. B* **1994**, *22* (2–3), 191–200.

(36) Chahal, R.; Starecki, F.; Doualan, J.-L.; Němec, P.; Trapananti, A.; Prestipino, C.; Tricot, G.; Boussard-Pledel, C.; Michel, K.; Braud, A.; Camy, P.; Adam, J.-L.; Bureau, B.; Nazabal, V. Nd^{3+}:Ga-Ge-Sb-S Glasses and Fibers for Luminescence in Mid-IR: Synthesis, Structural Characterization and Rare Earth Spectroscopy. *Opt. Mater. Express* **2018**, *8* (6), 1650.

(37) Golovchak, R.; Nazabal, V.; Bureau, B.; Oelgoetz, J.; Kovalskiy, A.; Jain, H. Chemical Order in Ga or Sb Modified Germanium Sulfide Glasses around Stoichiometry: High-Resolution XPS and Raman Studies. *J. Non. Cryst. Solids* **2018**, *499*, 237–244.

(38) Masselin, P.; Le Coq, D.; Cuisset, A.; Bychkov, E.; Fletcher, L. B.; Witcher, J. J.; Troy, N.; Reis, S. T.; Brow, R. K.; Vazquez, R. M.; Osellame, R.; Krol, D. M. Spatially Resolved Raman Analysis of Laser Induced Refractive Index Variation in Chalcogenide Glass. *Opt. Mater. Express, Vol. 2, Issue 12, pp. 1768-1775* **2012**, *2* (12), 1768–1775.

(39) Guignard, M.; Nazabal, V.; Smektala, F.; Adam, J. L.; Bohnke, O.; Duverger, C.; Moréac, A.; Zeghlache, H.; Kudlinski, A.; Martinelli, G.; Quiquempois, Y. Chalcogenide Glasses Based on Germanium Disulfide for Second Harmonic Generation. *Adv. Funct. Mater.* **2007**, *17* (16), 3284–3294.

(40) Pethes, I.; Nazabal, V.; Chahal, R.; Bureau, B.; Kaban, I.; Belin, S.; Jóvári, P. Local Motifs in GeS_2–Ga_2S_3 Glasses. *J. Alloys Compd.* **2016**, *673*, 149–157.

(41) Lucovsky, G.; Deneufville, J. P.; Galeener, F. L. Study of the Optic Modes of $Ge_{0.30}S_{0.70}$ Glass by Infrared and Raman Spectroscopy. *Phys. Rev. B* **1974**, *9* (4), 1591–1597.

(42) Heo, J.; Yoon, J. M.; Ryou, S. Y. Raman Spectroscopic Analysis on the Solubility Mechanism of La^{3+} in GeS_2–Ga_2S_3 Glasses. *J. Non. Cryst. Solids* **1998**, *238* (1–2), 115–123.

(43) Julien, C.; Barnier, S.; Massot, M.; Chbani, N.; Cai, X. AM Loireau-Lozac h, M. Guittard. *Mater. Sci. Eingineering B* **1994**, *22*, 191–200.

(44) Robinel, E.; Carette, B.; Ribes, M. Silver Sulfide Based Glasses (I). Glass Forming Regions, Structure and Ionic Conduction of Glasses in GeS_2-Ag_2S and GeS_2-Ag_2S-AgI Systems. *J. Non. Cryst. Solids* **1983**, *57* (1), 49–58.

(45) Wang, X. F.; Gu, S. X.; Yu, J. G.; Zhao, X. J.; Tao, H. Z. Structural Investigations of GeS_2-Ga_2S_3-CdS Chalcogenide Glasses Using Raman Spectroscopy. *Solid State Commun.* **2004**, *130* (7), 459–464.

(46) Verger, L.; Trébosc, J.; Furet, E.; Dénoue, K.; Zhang, J.; Cheviré, F.; Le Coq, D.; Calvez, L.; Lafon, O.; Hernandez, O. Mechanochemical Synthesis and Study of the Local Structure of $NaGaS_2$ Glass and Glass-Ceramics. *Inorg. Chem.* **2022**, *61* (46), 18476–18485.

(47) Yohannan, J. P.; Vidyasagar, K. Syntheses and Structural Characterization of Non-Centrosymmetric $Na_2M_2M'S_6$ (M, M′=Ga, In, Si, Ge, Sn, Zn, Cd) Sulfides. *J. Solid State Chem.* **2016**, *238*, 147–155.

(48) Bréhault, A.; Cozic, S.; Boidin, R.; Calvez, L.; Bychkov, E.; Masselin, P.; Zhang, X.; Le Coq, D. Influence of NaX (X=I or Cl) Additions on GeS_2-Ga_2S_3 based Glasses. *J. Solid State Chem.* **2014**, *220*, 238–244.

(49) Lin, C.; Qu, G.; Li, Z.; Dai, S.; Ma, H.; Xu, T.; Nie, Q.; Zhang, X. Correlation between Crystallization Behavior and Network Structure in GeS_2-Ga_2S_3-CsI Chalcogenide Glasses. *J. Am. Ceram. Soc.* **2013**, *96* (6), 1779–1782.

(50) Cozic, S.; Bréhault, A.; Le Coq, D.; Usuki, T. GeS_2–Ga_2S_3–LiCl Glass System: Electrical Conductivity and Structural Considerations. *Int. J. Appl. Glas. Sci.* **2016**, *7* (4), 513–523.

(51) Zhang, L.; Liu, F.; Brinkman, K.; Reifsnider, K. L.; Virkar, A. V. A Study of Gadolinia-Doped Ceria Electrolyte by Electrochemical Impedance Spectroscopy. *J. Power Sources* **2014**, *247*, 947–960.

(52) Barsoukov, E.; Macdonald, J. R. *Impedance Spectroscopy: Theory, Experiment, and Applications*;

2005.